Breaking the yield–selectivity trade-off in polystyrene waste valorization via tandem depolymerization and hydrogenolysis

Jia Wang, Zedong Zhang, Yan Zhang, Dongxian Li, Zechao Zhuang, Wei Liao, Tong Han, Lin Dong, Shule Wang, Dingsheng Wang, et al.

Breaking the Yield-Selectivity Trade-Off in Polystyrene Waste Valorization to Toluene via Thermodynamic Decoupling with Dilute Ru Catalysis

Jia Wang[1], Zedong Zhang[2*], Yan Zhang[2], Dongxian Li[1], Zechao Zhuang[2], Wei Liao[1], Tong Han[3], Lin Dong[1], Shule Wang[4*], Dingsheng Wang[2*], and Jianchun Jiang[1*]

[1] Jiangsu Co-Innovation Center for Efficient Processing and Utilization of Forest Resources, Nanjing Forestry University, Nanjing 210037, China

[2] Department of Chemistry, Tsinghua University, Beijing 100084, China

[3]Department of Materials Science and Engineering, KTH Royal Institute of Technology, SE 10044, Stockholm, Sweden

[4] Department of Environmental Science, Policy and Management, University of California, Berkeley, CA 94720, United States

*Corresponding author.

Email: zedong.zhang@northwestern.edu(Z. Z.); shule@berkeley.edu (S. W.); wangdingsheng@mail.tsinghua.edu.cn (D. W.); jiangjc@icifp.cn (J. J.).

Abstract

Converting plastic waste into sustainable toluene addresses plastic pollution and reduces the carbon footprint of conventional naphtha-derived aromatics. However, process viability remains limited due to the challenge of precise reaction control in complex multiphase systems and catalyst inefficiencies. Such limitations lead to low yields (<12 wt%) and poor selectivity (<13%), even under high pressures (4 MPa) and prolonged reaction times (16 h). Here, we report a vapor-phase hydrogenolysis strategy catalyzed by Ru single atoms on Co_3O_4 (Ru_{SA}/Co_3O_4), decoupling depolymerization from hydrogenolysis to overcome the yield–selectivity trade-off. In a pressurized dual-stage fixed-bed reactor, polystyrene waste undergoes hydropyrolysis at 475 °C followed by vapor-phase hydrogenolysis at 275 °C under

0.4 MPa H_2 (residence time: 2.4 s), yielding toluene with 99% selectivity, 83.5 wt% yield, and a formation rate of 1320 mmol $g_{cat.}^{-1}$ h^{-1}. The Ru_{SA}/Co_3O_4 catalyst demonstrates excellent stability, maintaining >99% conversion and selectivity during 100 h continuous operation with model intermediates (TON: 24,747), and effectively processes diverse real-world polystyrene wastes. Life cycle assessment indicates a 53% carbon footprint reduction over fossil-based methods, while techno-economic analysis estimates a competitive minimum selling price of $0.61/kg, well below the current industry benchmark of $1/kg. This selective and scalable technology provides a viable pathway for plastic waste valorization, promoting circular economy practices and supporting global sustainability goals.

Introduction

Aromatic hydrocarbons, such as benzene, toluene, and xylenes (BTX), are essential building blocks in the synthesis of chemicals, plastics, and fuels [1-4]. Currently, around 70% of BTX is produced from petrochemicals via catalytic naphtha reforming, contributing to 7% of global greenhouse gas emissions (Fig. 1a) [5, 6]. The rising demand for plastics exacerbates these environmental issues, with production projected to surpass 1,100 million tons by 2050 [7-10]. Despite recycling efforts, only 9% of plastic waste is recycled [11-15]. While mechanical recycling is common for polyesters, it faces challenges with polyolefins [16-19]. Converting plastic waste into aromatics supports circular economy goals by reducing both climate impact and dependence on fossil-derived feedstocks [20-22].

Recent studies have demonstrated various catalytic pathways for transforming polystyrene waste into functionalized aromatics, such as benzaldehyde, benzoic acid, and diphenylmethane via oxidative or photochemical strategies, as well as into bulk BTX compounds through hydrogenolysis or catalytic pyrolysis [23-26]. Among these products, toluene is of particular interest because of its central role in the petrochemical industry, with global demand exceeding 37 million tons per year and projected to reach 77 million tons by 2035 [27]. However, BTX-directed methods often result in broad product distributions and limited ability to tune selectivity, with toluene yields typically below 12 wt% and selectivity under 13% (Fig. 1b) [28-30]. A central challenge lies in controlling catalytic processes, particularly in multiphase (gas–solid–liquid) systems where the thermodynamic requirements of depolymerization and hydrogenation are inherently mismatched [31-33]. For instance, hydrogenolysis, typically conducted in a single high-pressure autoclave, presents two

critical issues. First, the thermodynamic mismatch between endothermic depolymerization and exothermic hydrogenation complicates process control. Second, as depolymerized products accumulate and raise system pressure, managing the interplay between pressure and temperature becomes increasingly difficult. Deconstruction is highly sensitive to temperature, whereas hydrotreating requires tight pressure control. Elevated pressure affects temperature stability, leading to a feedback loop that hinders process optimization. Furthermore, zeolite catalysts (e.g., ZSM-5) are commonly employed in the catalytic pyrolysis of plastic waste to produce aromatic hydrocarbons [34-38]. However, these catalysts typically yield a mixture of C_6–C_{13} aromatics, including both monocyclic and polycyclic compounds (Fig. 1b) [39-41]. Hence, advancements in catalytic strategies and process optimization are vital to achieving efficient and selective chemical transformation of plastic waste.

In this study, we report a tandem catalytic strategy that integrates hydropyrolysis with vapor-phase hydrogenolysis for the selective production of toluene from polystyrene waste. In this process, hydropyrolysis thermally depolymerizes polystyrene, while subsequent gas-phase hydrogenolysis cleaves the resulting intermediates over a solid catalyst. By transitioning from a conventional three-phase gas–liquid–solid system to a streamlined gas–solid flow, we decoupled depolymerization from hydrogenolysis, thereby enhancing reaction controllability, scalability, and overall efficiency (Fig. 1b). To further enhance toluene selectivity within this gas–solid system, we developed a ruthenium single-atom catalyst supported on cobalt oxide (Ru_{SA}/Co_3O_4). Owing to their maximized atomic utilization and tunable electronic structure, single-atom catalysts enable high activity and selectivity [42-48]. In particular, Ru_{SA}/Co_3O_4 was designed to selectively cleave C–C bonds in key intermediates, steering the reaction toward the formation of toluene. Under reaction conditions of 0.4 MPa and 275 °C in the second-stage hydrogenolysis reactor, the Ru_{SA}/Co_3O_4 demonstrated a toluene selectivity of 99%, with a yield of 83.5 wt% and a formation rate of 1320 mmol $g_{cat.}^{-1}$ h^{-1}. Furthermore, the catalyst exhibited remarkable stability, maintaining consistent performance over 100 cycles without noticeable deactivation. By efficiently converting plastic waste into high-value toluene, this method simplifies downstream separation and reduces energy input, offering a sustainable and cost-effective route for plastic waste management.

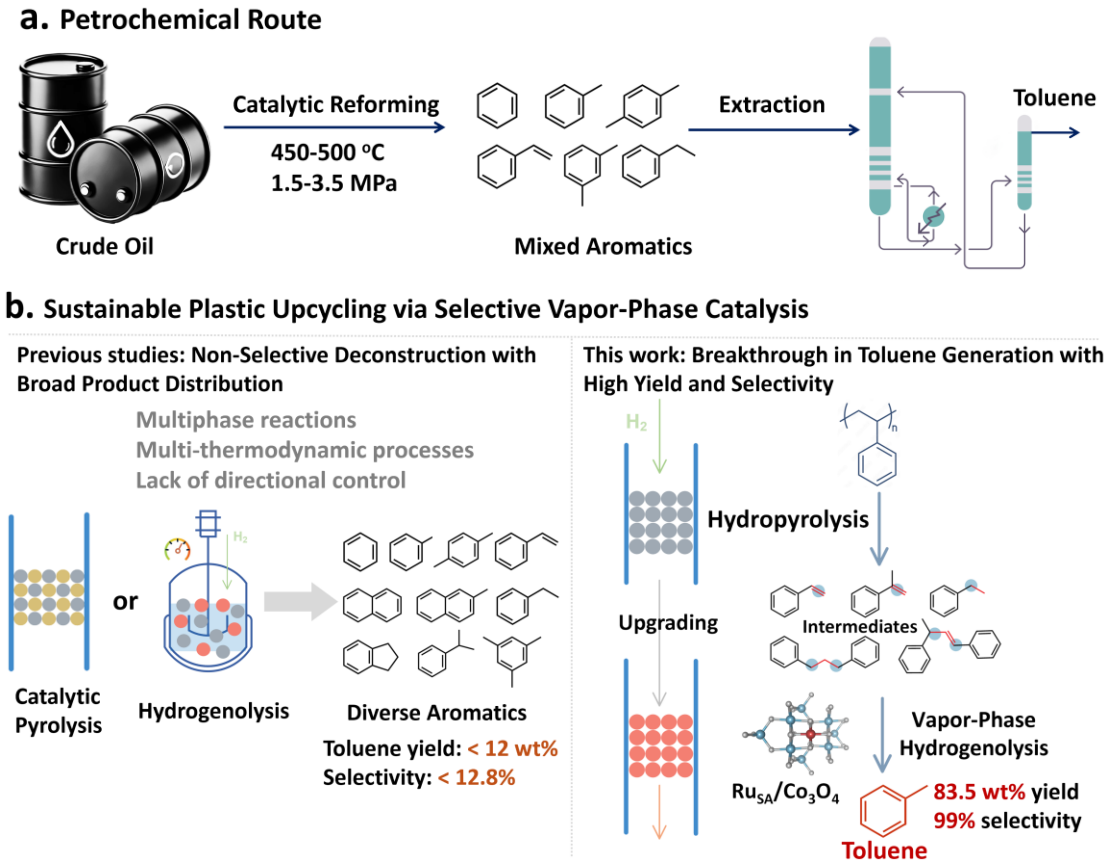

Fig. 1 | Pathways for toluene production from crude oil and polystyrene waste. a, Petrochemical route for mixed aromatic hydrocarbon production. Conventional catalytic reforming process for toluene production from crude oil, operating at 450–500 °C and 1.5–3.5 MPa, yielding a mixture of aromatic compounds followed by extraction to obtain toluene. **b,** Selective vapor-phase catalytic upgrading of plastic waste into high-purity toluene. Comparison between prior approaches yielding diverse aromatic products and the selective hydrogenolysis strategy in this work.

Catalyst Characterization

The cobalt basic carbonate precursor was initially synthesized using a hydrothermal method, followed by impregnation and air calcination to produce the Ru_{SA}/Co_3O_4 catalyst [10, 49-51]. Energy dispersive spectroscopy (EDS, Fig. 2a) confirmed the uniform distribution of many small Co_3O_4 nanoparticles, approximately 20 nm in size. Scanning electron microscopy (SEM) images showed that the synthesized Co_3O_4 exhibited a nanosheet morphology with sizes ranging from 500 to 1000 nm (Supplementary Fig. 1a). Transmission electron microscopy (TEM) images (Supplementary Fig. 1b, d) further revealed a lattice spacing of 0.467 nm, corresponding to the (111) plane of Co_3O_4. Additionally, a weak peak at 284.2 eV in the electron energy loss spectrum (EELS) was ascribed to the M_4 edge of Ru

(Supplementary Fig. 2), while a second peak at 543.5 eV corresponded to the O K edge. These findings confirm the successful incorporation of Ru atoms into the Co_3O_4 structure and suggest a strong interaction between Ru and oxygen species within the catalyst. We also prepared Ru nanoparticles on cobalt oxide (Ru_{NP}/Co_3O_4) for comparison with the single-atom Ru catalyst. This catalyst exhibited a similar structure and uniform Ru dispersion to the single-atom catalyst (Supplementary Fig. 3).

Phase analysis of the catalysts via X-ray diffraction (XRD) revealed that the Co_3O_4 structure (PDF#43-1003) remained unchanged, regardless of whether Ru single atoms (Ru_{SAs}) or Ru nanoparticles (Ru_{NPs}) were present as active sites (Supplementary Figs. 4-5 and Supplementary Tables 1-2). High-resolution transmission electron microscopy (HRTEM) was employed to further examine the microstructure. Aberration-corrected HAADF-STEM imaging (Fig. 2b) visualized the Ru single atoms, and slight rotation of the (111) plane during imaging enhanced the clarity of the Ru atom distribution. High-contrast spots, highlighted by blue circles in the magnified image (Fig. 2c), represent the single Ru atoms dispersed on the Co_3O_4 nanosheets. No evidence of Ru atom aggregation was observed, confirming successful dispersion.

We characterized the electronic structure of the Ru_{SA}/Co_3O_4 catalyst using X-ray photoelectron spectroscopy (XPS) to explore the interaction between Ru_{SAs} and the Co_3O_4 support. In the high-resolution Co 2p spectrum (Supplementary Fig. 6), an increase in binding energy for both the $2p_3/_2$ and $2p_1/_2$ peaks indicated charge transfer between Ru and Co, with Ru oxidizing some Co sites and increasing the Co^{3+} component (Supplementary Table 3) [52, 53]. However, no significant differences in the electronic state of Co were observed between Ru_{SAs} and Ru_{NPs}. The high-resolution O 1s spectrum revealed that the single-atom Ru catalyst has a lower defect oxygen content compared to the support, resulting from its coordination with oxygen vacancies in Co_3O_4. In contrast, Ru_{NPs} increased surface oxygen defects, because their larger size alters interactions with the support. The Ru 3p spectrum revealed that the $3p_1/_2$ peak for Ru_{SAs} appeared at 463.8 eV, higher than the typical 461 eV for Ru (0), confirming the oxidized state of Ru within the Co_3O_4 substrate.

We used X-ray absorption spectroscopy (XAS) to examine the oxidation state of Ru, based on the absorption edge position (Fig. 2d). In the Ru_{SAs} catalyst, Ru exhibits a +3 oxidation state, while in Ru_{NPs}, it remains in a zero-oxidation state. The XANES spectra reveal that the white line peak and near-edge absorption reflect multiple scattering effects around the central Ru atoms. Comparable to Ru foil, the Ru_{NPs}

exhibit a near-edge adsorption peak shape but with diminished intensity, a consequence of their smaller particle size and unsaturated coordination structure. In contrast, the Ru_{SAs} display a near-edge peak distinct from both Ru foil and RuO_2, indicating a unique Ru coordination environment. To validate the structural and electronic insights from XANES, we performed FEFF9 simulations based on a single-atom Ru model, which accurately reproduced the experimental near-edge features (Supplementary Fig. 7a). Partial density of states (PDOS) analysis attributes the higher-energy spectral feature to Ru–Co electronic interactions, underscoring the role of Ru–O–Co coordination in shaping the XANES response (Supplementary Fig. 7b).

A detailed analysis of the single-scattering signal in the EXAFS (Extended X-ray Absorption Fine Structure) region, processed with K^2-weighting, reveals coordination differences between Ru_{SAs} and the reference sample (Supplementary Fig. 8). In the high-K region ($K > 8$ $Å^{-1}$), reduced peak intensity indicates long-range disorder in the Ru atomic arrangement, particularly in the third coordination shell, confirming the absence of Ru-based compound formation and aligning with the design of single-dispersed Ru sites. R-space transformation of the Ru_{SAs} spectrum shows two prominent peaks at approximately 1.5 Å and 2.4 Å (Fig. 2e). The first peak corresponds to Ru-O coordination, while the second is attributed to long-range Ru-Co interactions, with the Ru-Co distance exceeding that of typical Ru-Ru bonding. Based on R-space curve analysis and morphology characterization, we proposed a Ru/Co_3O_4 (111) model (Fig. 2f). Fitting this model to the R-space curves using IFEFFIT revealed a coordination number of approximately 5-fold for Ru-O and 9-fold for the Ru-Co second coordination shell, suggesting the presence of Co vacancies in the support (Supplementary Table 4). Wavelet transform analysis (Supplementary Fig. 9), integrating both K-space and R-space data, further supports the proposed structure and curve interpretation.

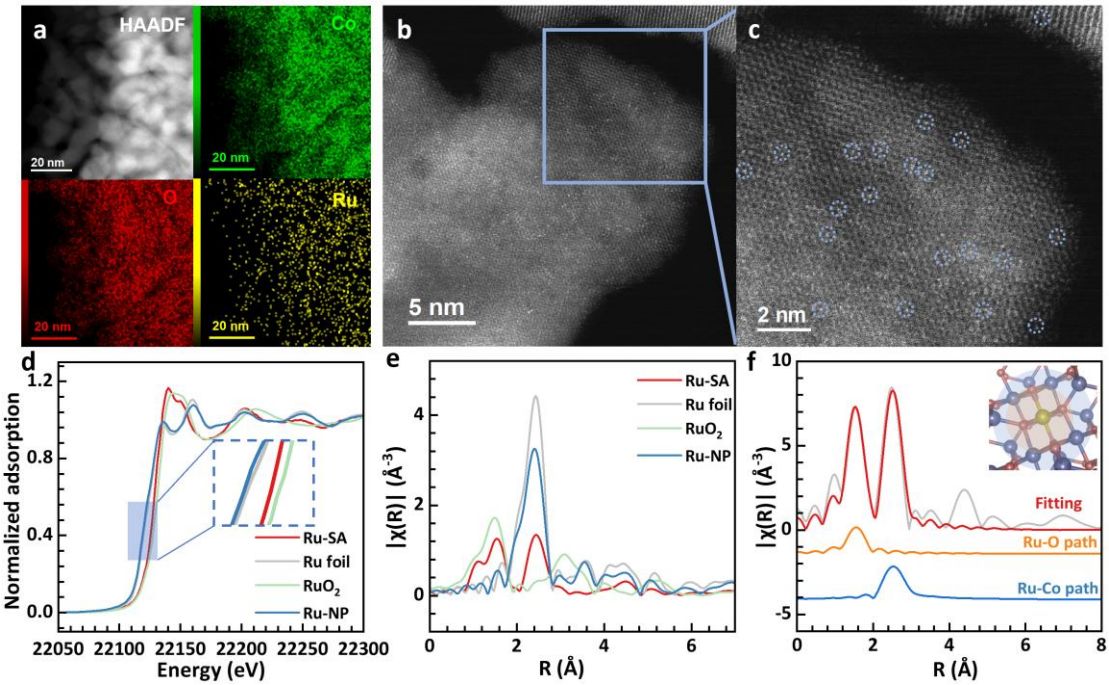

Fig. 2 | Structural and electronic characterization. a, EDS mapping images of Ru_{SA}/Co_3O_4 (green represent Co element, red represent O, and yellow represent Ru element. **b,** Atomic-scale structure of Ru_{SA}/Co_3O_4. HAADF-STEM image of Ru_{SA}/Co_3O_4 with a scale bar of 5 nm. **c,** Enlarged region in **2b** with blue circles marking the locations of Ru atoms, the scale bar of 2 nm. **d,** Normalized XANES spectra of the Ru K-edge. **e,** R-space EXAFS spectra of Ru_{SA}/Co_3O_4 and reference materials. **f,** EXAFS fitting results for Ru_{SA}/Co_3O_4. Inset depicting the model used for fitting with two coordination shells.

Catalytic Activity

We investigated the selective vapor-phase hydrogenolysis of styrene, the monomer of polystyrene, to produce toluene using various catalysts. The experiments were conducted in a pressurized dual-stage fixed-bed reactor, where styrene was vaporized in the first stage and subjected to hydrogenolysis in the second stage at 275 °C and 0.4 MPa (Supplementary Figs. 10–12). Among all catalysts investigated, Co_3O_4 achieved a 66.4% conversion of styrene, with ethylbenzene as the major product (92.5% selectivity) and only 7.5% toluene (Fig. 3a). This result indicates that Co_3O_4 can promote the hydrogenation of the vinyl group (–CH=CH_2) in styrene to form ethylbenzene, but has poor activity to cleave the C_{sp3}-C_{sp3} bond in ethylbenzene to produce toluene.

Introducing Ru nanoparticles on Co_3O_4 (Ru_{NP}/Co_3O_4) significantly enhanced the catalytic performance, increasing styrene conversion to 87.9%. The main products were benzene (60.3% selectivity) and ethylbenzene (38.9%), suggesting that

Ru_{NP}/Co_3O_4 promote the cleavage of the C_{sp2}-C_{sp3} bond between the benzene ring and the ethyl group in ethylbenzene. Remarkably, dispersing ruthenium as single atoms on Co_3O_4 (Ru_{SA}/Co_3O_4) led to complete conversion of styrene and a significant shift in selectivity. It gave an exceptional selectivity of toluene (>99%) among the aromatic hydrocarbons, demonstrating its high efficiency in transforming the vinyl group of styrene into a methyl group. Chromatograms in Fig. 3b show only a single toluene peak with Ru_{SA}/Co_3O_4, indicating that no other aromatic byproducts were detected. This contrasts with other catalysts, which produce multiple peaks corresponding to diverse products such as benzene and ethylbenzene. For comparison, a commercial 5 wt% Ru/Al_2O_3 catalyst also achieved complete styrene conversion but predominantly hydrogenated the benzene ring, yielding 40.3% ethylcyclohexane, 54.8% ethylbenzene, and only 1.7% toluene (Fig. 3a).

The selective hydrogenolysis of Ru_{SA}/Co_3O_4 was further evaluated using additional common products from polystyrene depolymerization, including ethylbenzene, methylstyrene, and C_{15}/C_{16} dimers, besides styrene. As shown in Fig. 3c, complete conversion of each substrate was achieved, with toluene as the primary product (over 92% selectivity) and ethylbenzene as the only minor aromatic byproduct. These results underscore the efficiency of Ru_{SA}/Co_3O_4 in facilitating selective C_{sp3}–C_{sp3} bond cleavage between the benzyl group and the alkyl side chains, highlighting its potential for converting polystyrene into toluene.

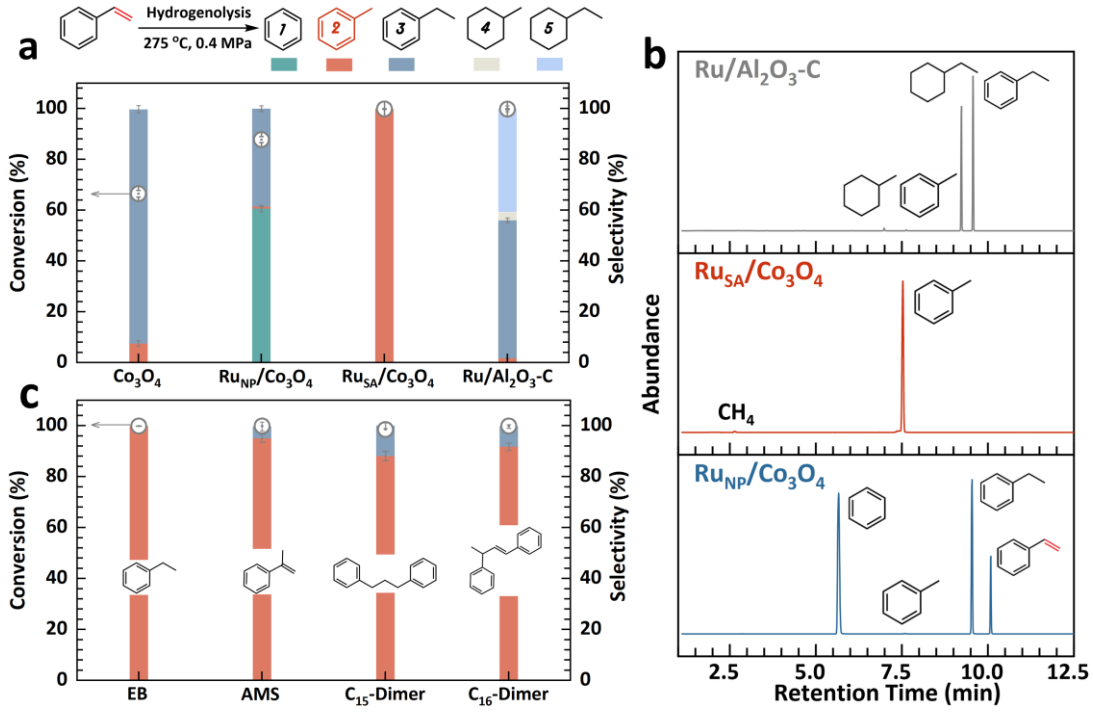

Fig. 3 | Catalytic vapor-phase hydrogenolysis of model compounds representative of polystyrene depolymerization intermediates. a, Conversion and selectivity

profiles for styrene hydrogenolysis over different catalysts. **b,** Total ion chromatograms of products obtained from hydrogenolysis of styrene over different catalysts. **c,** Vapor-phase hydrogenolysis performance on additional polystyrene-derived substrates over Ru_{SA}/Co_3O_4 catalyst. Selectivity values represent the distribution of aromatic hydrocarbon products and exclude gaseous byproducts such as methane. The vapor-phase hydrogenolysis was conducted at 275 °C and 0.4 MPa. Catalyst loading was 30 mg, with a catalyst-to-feedstock mass ratio of 10:1. Error bars represent standard deviation (SD, n = 3). Error bars smaller than the symbols or bars indicate minimal variation and excellent reproducibility.

We further examined the tandem conversion of polystyrene (PS, Mw = 192 kDa; Supplementary Figs. 13-15, Supplementary Table 5) to toluene in the same reactor. In the first stage, PS underwent hydropyrolysis, yielding unstable aromatic intermediates such as styrene and its dimers. To prevent polymerization and stabilize these intermediates, the second stage employed online vapor-phase hydrogenolysis, selectively converting them into toluene. This integrated process significantly enhances energy efficiency by eliminating the need for condensation and reheating steps, which are typically required in conventional pyrolysis followed by liquid-phase hydrogenation (Supplementary Fig. 16a). By avoiding these energy-intensive stages, our method reduces overall energy consumption, thereby contributing to a significant reduction in carbon emissions. Furthermore, gas-solid hydrogenolysis improves mass transfer and facilitates precise reaction control, allowing for better adjustment of product selectivity. In contrast to the multiphase systems (i.e., gas-solid-liquid) of traditional methods (Supplementary Fig. 16b), this approach enhances scalability and the ability to fine-tune product outcomes.

Our optimization studies using the Ru_{SA}/Co_3O_4 catalyst identified key parameters influencing toluene yield and selectivity. Increasing the hydropyrolysis temperature in the first-stage reactor from 425 °C to 475 °C enhanced the toluene yield from 56.3 wt% to a peak of 83.5 wt% (Supplementary Fig. 17). However, temperatures above 475 °C did not yield further improvements. Temperature control in the second-stage vapor-phase hydrogenolysis reactor was equally crucial. At 200 °C, the toluene yield was limited to 40.5 wt%, accompanied by notable byproducts such as ethylbenzene and ethylcyclohexane (Supplementary Figs. 18-19). Raising the temperature to 275 °C increased the yield to its peak value, favoring toluene formation. Conversely, increasing the temperature to 350 °C resulted in excessive cracking, with methane becoming the predominant product (97.3 wt% yield, Supplementary Figs. 20-21). Higher reaction pressures (1.0 MPa) during vapor-phase hydrogenolysis suppressed

toluene formation, favoring cycloalkanes like methylcyclohexane (MCH), which achieved 90.1% selectivity (Supplementary Figs. 22-24). Notably, MCH serves as both a liquid hydrogen carrier and a high-density aviation fuel, highlighting the versatility of this integrated waste-to-value approach.

Mass balance analysis at a hydropyrolysis temperature of 475 °C, a vapor-phase hydrogenolysis temperature of 275 °C, and a reaction pressure of 0.4 MPa showed that the products of PS hydropyrolysis were distributed across gas, liquid, and solid phases (Fig. 4a). The liquid products dominated the yield, accounting for 94 wt% of the total. Without a catalyst, styrene was the major component with a high selectivity of 89.7%, along with minor contributions from toluene (2.7%), ethylbenzene, methylstyrene, and heavier aromatic compounds such as C_{15} and C_{16} dimers (Fig. 4b, Supplementary Fig. 25). The introduction of catalysts significantly influenced product distribution. Co_3O_4 primarily converted PS to ethylbenzene through direct hydrogenation of the vinyl group in styrene, achieving a selectivity of 60.3%. In contrast, Ru_{NP}/Co_3O_4 favored benzene (62.3%) and ethylbenzene (31.4%) production. Remarkably, Ru_{SA}/Co_3O_4 achieved near-complete selectivity for toluene with a substantial yield of 83.5 wt%. A comparable yield of 82.9 wt% was also obtained under scale-up conditions with liquid-phase product collection, confirming the robustness of the catalytic performance (Supplementary Figs. 26-27). This high specificity arises from the ability of the catalyst to precisely cleave the C_{sp3}-C_{sp3} bonds within the vinyl group while preserving the C_{sp2}-C_{sp3} bond, thereby minimizing the formation of byproducts.

The performance of Ru_{SA}/Co_3O_4 was compared to that of ZSM-5, a widely used catalyst in the catalytic pyrolysis of plastics for producing aromatic hydrocarbons [19, 54]. ZSM-5 yielded aromatic compounds with carbon chain lengths ranging from C_6 to C_{12}; however, it generated only 1.4% toluene while producing 12.2% polycyclic aromatic hydrocarbons (Supplementary Fig. 28), which pose significant environmental risks because of their toxicity and persistence [55]. The wide product distribution underscores the challenges of conventional aromatization pathways in directing selectivity towards toluene. We also evaluated our results against previous studies on PS hydrogenolysis. Under Ru_{SA}/Co_3O_4 catalysis at 0.4 MPa, with a calculated reaction time of 2.4 s, our process achieved an 8.4-fold increase in yield (83.5 *vs.* 11.9 wt%) and a 7.8-fold improvement in selectivity (99.9 *vs.* 12.8%) compared to the best-reported values obtained under more stringent conditions (1 MPa for 6 h, Supplementary Tables 6-8) [56].

We demonstrated the scalability of Ru_{SA}/Co_3O_4 by testing it on nine different post-consumer single-use PS wastes (Fig. 4c, Supplementary Figs. 29-30). The catalyst consistently produced approximately 81 wt% toluene across all tested materials, with toluene selectivity exceeding 99% and a formation rate of 1320 $mmol \cdot g_{cat.}^{-1} \cdot h^{-1}$. The instant noodle container (INC) sample exhibited comparable toluene yield and selectivity despite containing red dye, suggesting negligible dye interference that may be attributed to thermal decomposition during hydropyrolysis (475 °C) and hydrogenolysis (275 °C). Furthermore, for nitrogen-containing plastic wastes such as acrylonitrile styrene (AS), Ru_{SA}/Co_3O_4 significantly enhanced hydrodenitrogenation and selective hydrogenolysis, achieving a toluene selectivity of 92.7% while effectively eliminating harmful byproducts including acrylonitrile, commonly observed in non-catalytic processes (Supplementary Figs. 31-32). In addition, the system exhibited strong compatibility with halogen-containing PS waste from construction insulation materials, including post-consumer expanded (EPS), extruded (XPS), and their mixtures. In all cases, high liquid yields (~80 wt%) and toluene selectivity above 97% were maintained (Supplementary Fig. 33). This excellent feedstock flexibility is also applicable to real-world mixed PS waste, maintaining a toluene selectivity above 99% (Supplementary Fig. 34).

To assess the durability and scalability of Ru_{SA}/Co_3O_4 under continuous-flow conditions (Supplementary Fig. 35), we performed a 100-hour vapor-phase hydrogenolysis using ethylbenzene as a model compound representative of intermediates formed during PS degradation. Ethylbenzene was selected over styrene due to the latter's tendency to polymerize under reaction conditions. The reaction was conducted in a fixed-bed reactor at 275 °C and 0.4 MPa with a weight hourly space velocity (WHSV) of 2.6 h^{-1}. Ru_{SA}/Co_3O_4 maintained excellent performance throughout the test, with >99.9% conversion and >99% selectivity toward toluene (Supplementary Fig. 36). The high turnover number (TON) of 24,747 reflects the robustness of the catalyst and its potential for industrial-scale application.

However, the low melting points of plastics hinder continuous feeding. In fixed-bed pyrolysis systems, radiant heating often causes premature softening of the feed, leading to screw feeder blockages and unstable operation. Most studies therefore assess catalyst stability using regeneration cycles rather than continuous feeding (Supplementary Table 9) [27, 57]. To address this challenge and simulate continuous industrial operation with actual polymer feedstocks, we adopted an intermittent feeding strategy, introducing polystyrene into a first-stage reactor periodically, while

the Ru_{SA}/Co_3O_4 catalyst remained stationary in the second-stage fixed-bed reactor for vapor-phase hydrogenolysis. Under these conditions, the catalyst consistently achieved 83 wt% yield of toluene with >99% selectivity across 100 repeated feed cycles (Fig. 4d), confirming its long-term operational stability and compatibility with realistic plastic waste streams. Post-reaction Raman and thermogravimetric analysis (TGA) indicated negligible coke formation, and further characterizations confirmed that the Ru single-atom structure remained unchanged (Supplementary Figs. 37–39).

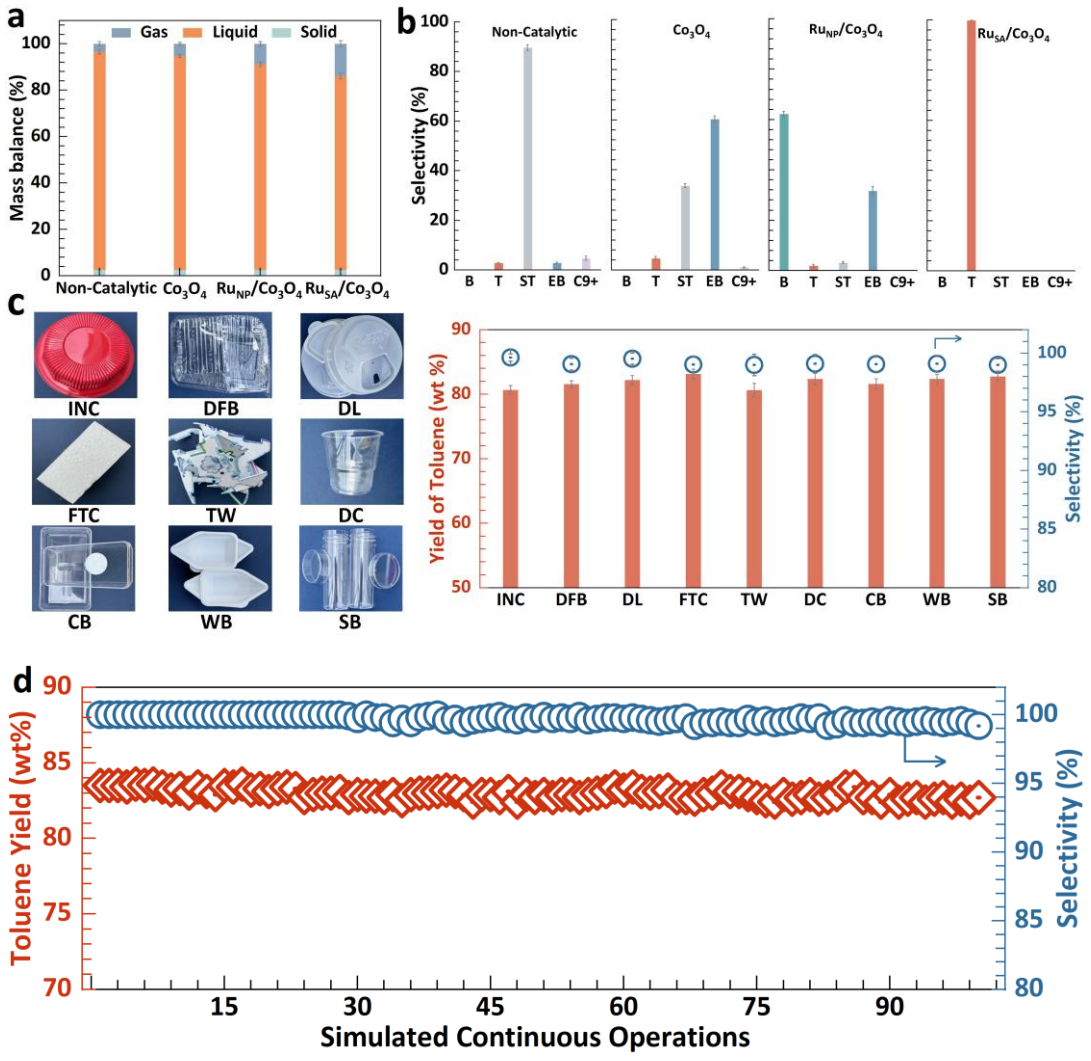

Fig. 4 | Tandem Valorization of polystyrene (PS) into toluene. a, Mass distribution across gas, liquid, and solid phases in non-catalytic and catalytic processes at a hydropyrolysis temperature of 475 °C, hydrogenolysis temperature of 275 °C, and reaction pressure of 0.4 MPa. Each reaction used 30 mg of catalyst with a catalyst-to-PS mass ratio of 10:1. The H_2 flow rate was set at 100 mL/min, corresponding to a reaction time of 2.4 s under standard conditions. **b,** Product distribution from PS depolymerization. Selectivity toward benzene (B), toluene (T), styrene (ST), ethylbenzene (EB), and C_{9+} products across different catalysts. **c,** Scalability testing

with post-consumer single-use PS wastes, including an instant noodle container (INC), disposable food box (DFB), drink lid (DL), foam takeout container (FTC), toy waste (TW), disposable cup (DC), cake box (CB), weighing boat (WB), and sample bottle (SB). **d,** Stability of Ru_{SA}/Co_3O_4 under simulated continuous PS feed.

Reaction Mechanism and Sustainability Evaluation

To examine the mechanisms driving high styrene conversion and toluene selectivity in Ru_{SA}/Co_3O_4 catalysts, we conducted density functional theory (DFT) calculations. The electronic structures of Ru single atoms and nanoparticles on Co_3O_4 directly influence the intermediates formed during the hydrogenolysis of styrene. Using d-band center theory, which correlates electronic properties with catalytic activity, we determined that the Co_3O_4 support in Ru single atoms shifts the 3d Fermi level of Ru to –1.3 eV, whereas it is –1.9 eV in Ru nanoparticles (Supplementary Figs. 40-42). Hybridization among Ru 4d, Co 3d, and O 2p orbitals in Ru_{SA}/Co_3O_4 suggests that coordination influences the electronic environment around active Ru sites, resulting in distinct adsorption behaviors compared to Ru_{NP}/Co_3O_4. The electron density difference revealed positive formal charges between Ru and its coordinated Co atoms, indicating a tendency for electron transfer from Ru to Co. This electron migration enhances the activity by facilitating the adsorption and activation of reactants on the active sites.

We evaluated the Gibbs free energies for four transition states involved in styrene hydrogenolysis. Ru_{SA}/Co_3O_4 exhibits a lower energy barrier of 2.38 eV in the hydrogenation of the vinyl group in styrene (ph-C_2H_4* + H*, TS2, Fig. 5a), compared to 2.78 eV for Ru_{NP}/Co_3O_4. This indicates that Ru_{SA}/Co_3O_4 has a lower energy barrier in the rate-determining step of vinyl group reduction. Following the hydrogenation of styrene to ethylbenzene, the adsorbed ph-C_2H_5* species at the catalyst interface undergoes C–C cleavage via hydrogenolysis to form toluene (Supplementary Fig. 42). The Co_3O_4 support exhibited a high energy barrier of 2.37 eV for ethylbenzene hydrogenolysis (ph-C_2H_5* + H* → ph-CH_3* + CH_3*, TS3). This barrier was reduced to 1.18 eV by Ru_{NP}/Co_3O_4 and further decreased to 0.59 eV with Ru_{SA}/Co_3O_4, highlighting the superior activity of single-atom Ru sites for this transformation (Supplementary Tables 10-12).

To elucidate the superior toluene selectivity of single-atom Ru compared to Ru nanoparticles, we calculated the adsorption energies of toluene intermediates and their subsequent reactions with H* (Supplementary Fig. 43). The toluene intermediate exhibited stronger adsorption on Ru nanoparticles (−0.80 eV) than on single-atom Ru

(−0.51 eV), suggesting that toluene adsorption is less favorable on the single-atom sites. Additionally, we conducted a transition state energy barrier analysis for the hydrogenolysis of toluene to benzene. The energy barrier for the key transition state (ph-CH_3* + H* → ph* + CH_3*, TS4) was markedly lower on Ru nanoparticles (1.32 eV) than on single-atom Ru (3.32 eV), indicating that hydrogenolysis of toluene to benzene is less favorable on single-atom Ru compared to nanoparticles. Overall, Ru nanoparticles exhibit a lower energy barrier for toluene hydrogenolysis and a higher barrier for ethylbenzene hydrogenolysis, leading to the formation of a broader range of products during PS depolymerization and thus reducing toluene selectivity.

The life cycle assessment (LCA) of the waste-to-toluene production evaluates the environmental footprint and sustainability of this circular transformation by quantifying cradle-to-gate emissions (Supplementary Fig. 44, Supplementary Tables 13–16). This LCA focuses on the global warming potential (GWP) across a 100-year horizon, yielding a value of 0.58 kg CO_2 equivalence (CO_2-eq) per kg of toluene produced, a 53% reduction compared to the petroleum-based toluene benchmark of 1.23 kg CO_2-eq/kg (Fig. 5b). Emission contributions from key process elements, including utilities, feedstock logistics, and transportation, were analyzed, identifying utilities as the largest contributor to GWP. This finding underscores the opportunity for carbon emission mitigation within utility operations, such as integrating renewable energy sources, to enhance overall environmental performance.

In tandem with the LCA, a techno-economic analysis (TEA) was conducted to assess the economic viability of establishing a dedicated facility in Shanghai, China, capable of processing the entire accessible feedstock. This analysis applied a discounted cash flow (DCF) framework to determine the minimum viable selling price required to sustain the integrated plastic-waste valorization process (Supplementary Tables 17–19). The capital expenditure (CAPEX) analysis highlighted significant investments in pyrolysis and hydrotreating units, marking these as primary cost drivers (Fig. 5c). Additional indirect costs, such as engineering and contingencies, further influenced CAPEX. The operating cost (OPEX) analysis revealed that hydrogen consumption was the primary cost driver when priced at the green hydrogen rate, while catalyst and utility expenses dominated when calculated with the grey hydrogen rate (Fig. 5d). This distinction emphasizes the energy-intensive and catalyst-dependent nature of the process across different hydrogen pricing assumptions. Feedstock, labor, and maintenance are also key cost elements, each contributing significantly to operational expenses.

An evaluation of the minimum selling price (MSP) of plastic-derived toluene showed a sensitivity to hydrogen pricing: the MSP increases to $1.22/kg with green hydrogen and decreases to $0.61/kg with grey hydrogen, both remaining competitive compared to the commercial toluene price of $1/kg (Fig. 5e, Supplementary Fig. 45, Supplementary Tables 20-22). These scenarios highlight the economic advantage of plastic-derived toluene over fossil-based alternatives, reinforcing the economic feasibility of this sustainable pathway. To further enhance economic and environmental sustainability, future developments should consider optimizing hydrogen sourcing and energy integration strategies, thus supporting scalable waste-to-toluene processes that can transition the chemical industry towards greener, circular economy frameworks.

Taken together, the demonstrated catalyst stability, gas-phase reaction configuration, and favorable TEA/LCA results highlight the practical potential of this strategy for industrial plastic waste valorization. The fully vapor-phase system simplifies product separation and process integration, while the selective production of toluene enables compatibility with existing petrochemical supply chains. These features make the approach not only scientifically robust, but also operationally scalable under real-world conditions.

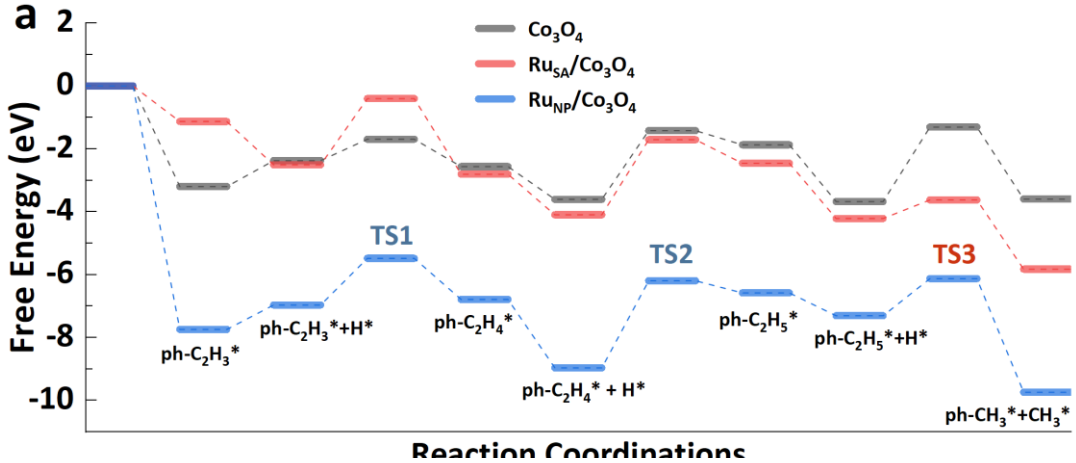

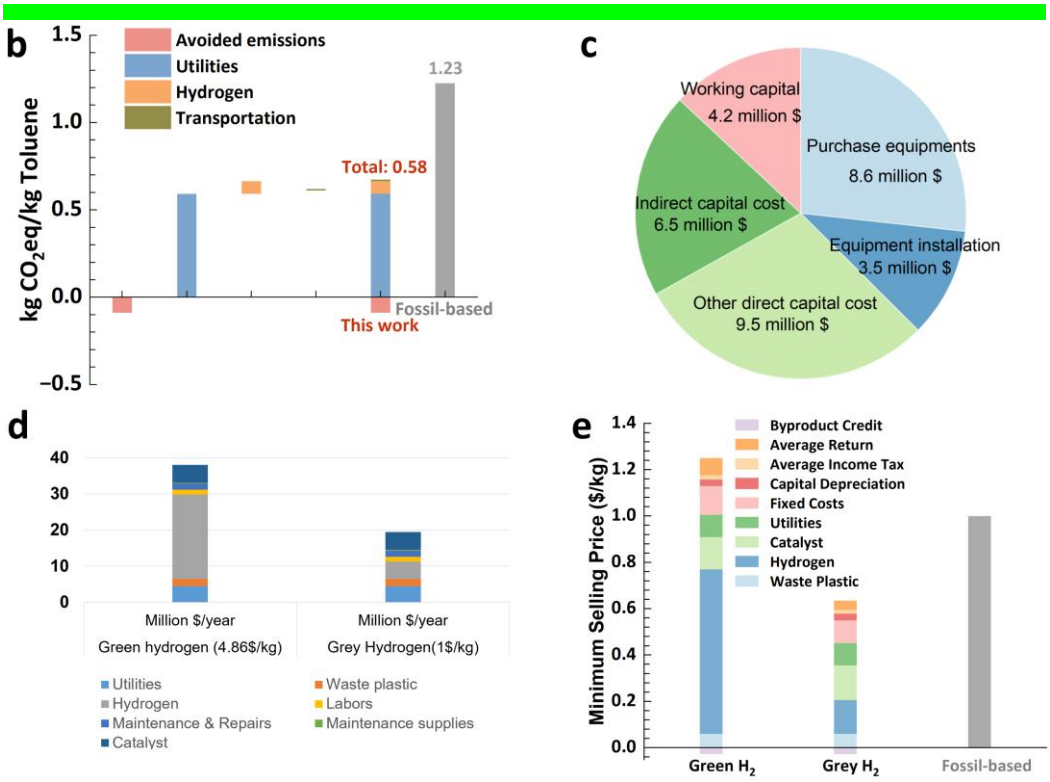

Fig. 5 | DFT mechanistic study, life cycle assessment (LCA), and techno-economic analysis (TEA) of sustainable toluene production from polystyrene waste. a, Free energy profiles of reaction pathways for key reaction steps on Co_3O_4, Ru_{SA}/Co_3O_4, and Ru_{NP}/Co_3O_4 catalysts. **b,** Life-cycle emissions for toluene production. Greenhouse gas emissions per kg of toluene produced, showing reductions achieved in this work compared to fossil-based methods. **c,** Capital cost distribution. Breakdown of capital investment for toluene production from PS, including contributions from working capital, equipment purchase, installation, indirect costs, and other direct costs. **d,** Operating cost comparison. Annual operating costs for toluene production using green hydrogen (4.86 $/kg) and grey hydrogen (1 $/kg), detailing costs for utilities, hydrogen, waste plastic, catalyst, and maintenance. **e,** Minimum selling price of toluene. Comparison of the minimum selling price of toluene produced with green hydrogen, grey hydrogen, and fossil-based processes, considering costs and byproduct credits.

Conclusions

This study presents a highly efficient strategy for the selective valorization of polystyrene waste into toluene using a Ru single-atom catalyst supported on Co_3O_4, offering significant advantages in catalytic activity and selectivity compared to traditional Ru-based methods. The developed vapor-phase hydrogenolysis process, operated at 0.4 MPa and 275 °C in the hydrogenolysis stage, achieves exceptional

toluene selectivity and yield by decoupling depolymerization from hydrogenolysis and simplifying the reaction system. Mechanistic studies reveal that the atomic dispersion of Ru plays a critical role in promoting selective C–C bond cleavage with significantly reduced energy barriers, outperforming conventional Ru nanoparticles. In addition, the catalyst sustained over 99% conversion and selectivity during 100 hours of continuous vapor-phase operation, achieving a turnover number of 24,747, which demonstrates its robustness and potential for scale-up. Furthermore, life cycle and techno-economic assessments highlight the sustainability and economic feasibility of this approach, demonstrating a 53% reduction in carbon footprint compared to petroleum-based processes and significant cost benefits, including a reduction in the minimum selling price of toluene to $0.61/kg when using grey hydrogen. These results establish this method as a promising solution for plastic waste management and aromatic production.

Acknowledgments:

This work was supported by the National Natural Science Foundation of China (52376195 to J. W. and 22171157 to D. W.). We also thank the BL11B station of Shanghai Synchrotron Radiation Facility (SSRF) measurement for providing beam time to support this work.

Author contributions:

Conceptualization: J. J., and D. W. Supervision: J. J., and D. W.; Methodology: J. W., Z. Z., Y. Z., W. L., and D. L.; Investigation: Z. Z., J. W., T. H., and S. W.; Theoretical calculation: Z. Z., D. L., and S. W.; Morphology characterization: L. D., Z. Z.; Writing-original draft: J. W., and Z. Z.; Writing-review and editing: D. W., and J. J.

Competing interests:

The authors declare no competing interests.

Supplementary materials:

Materials and Methods, Supplementary Figs. 1 to 45, Tables 1 to 22.

Data and materials availability:

All data are available in the main text or the supplementary materials.

Correspondence and requests for materials should be addressed to Jianchun Jiang,

Dingsheng Wang, Shule Wang, or Zedong Zhang.

References

1. Stone, M.L. et al. Continuous hydrodeoxygenation of lignin to jet-range aromatic hydrocarbons. *Joule* **6**, 2324-2337 (2022).
2. Hussain, I. et al. Chemical Upcycling of Waste Plastics to High Value-Added Products via Pyrolysis: Current Trends, Future Perspectives, and Techno-Feasibility Analysis. *Chem. Rec.* **23**, e202200294 (2023).
3. Wu, Y. et al. Benzene, Toluene, and Xylene (BTX) Production from Catalytic Fast Pyrolysis of Biomass: A Review. *ACS Sustainable Chem. Eng.* **11**, 11700-11718 (2023).
4. Kasipandi, S. & Bae, J.W. Recent Advances in Direct Synthesis of Value-Added Aromatic Chemicals from Syngas by Cascade Reactions over Bifunctional Catalysts. *Adv. Mater.* **31**, e1803390 (2019).
5. Miao, D. et al. Selective Synthesis of Benzene, Toluene, and Xylenes from Syngas. *ACS Catal.* **10**, 7389-7397 (2020).
6. Dossow, M. et al. Electrification of gasification-based biomass-to-X processes – a critical review and in-depth assessment. *Energy Environ. Sci.* **17**, 925-973 (2024).
7. Li, L. et al. Converting Plastic Wastes to Naphtha for Closing the Plastic Loop. *J. Am. Chem. Soc.* **145**, 1847-1854 (2023).
8. Yadav, G. et al. Techno-economic analysis and life cycle assessment for catalytic fast pyrolysis of mixed plastic waste. *Energy Environ. Sci.* (2023).
9. Wang, M. et al. Complete hydrogenolysis of mixed plastic wastes. *Nat. Chem. Eng.* **1**, 376-384 (2024).
10. Zhang, Z. et al. Mixed Plastics Wastes Upcycling with High-Stability Single-Atom Ru Catalyst. *J. Am. Chem. Soc.* **145**, 22836-22844 (2023).
11. Zhao, B. et al. Selective Upcycling of Polyolefins into High-Value Nitrogenated Chemicals. *J. Am. Chem. Soc.* (2024).
12. Jaydev, S.D., Martín, A.J., Garcia, D., Chikri, K. & Pérez-Ramírez, J. Assessment of transport phenomena in catalyst effectiveness for chemical polyolefin recycling. *Nat. Chem. Eng.* (2024).
13. Jaydev, S.D., Martin, A.J. & Perez-Ramirez, J. Direct Conversion of Polypropylene into Liquid Hydrocarbons on Carbon-Supported Platinum Catalysts. *ChemSusChem* **14**, 5179-5185 (2021).
14. Ellis, L.D. et al. Chemical and biological catalysis for plastics recycling and upcycling. *Nat. Catal.* **4**, 539-556 (2021).
15. Jie, X. et al. Microwave-initiated catalytic deconstruction of plastic waste into hydrogen and high-value carbons. *Nat. Catal.* **3**, 902-912 (2020).
16. Wu, X. et al. Polyethylene Upgrading to Liquid Fuels Boosted by Atomic Ce Promoters. *Angew Chem Int Ed Engl* **63**, e202317594 (2024).

17. Kots, P.A., Vance, B.C., Quinn, C.M., Wang, C. & Vlachos, D.G. A two-stage strategy for upcycling chlorine-contaminated plastic waste. *Nat. Sustainability* (2023).
18. Conk, R.J. et al. Polyolefin waste to light olefins with ethylene and base-metal heterogeneous catalysts. *Science* **385**, 1322-1327 (2024).
19. Duan, J. et al. Coking-Resistant Polyethylene Upcycling Modulated by Zeolite Micropore Diffusion. *J. Am. Chem. Soc.* **144**, 14269-14277 (2022).
20. Du, J. et al. Efficient solvent- and hydrogen-free upcycling of high-density polyethylene into separable cyclic hydrocarbons. *Nat. Nanotechnol.* (2023).
21. Xu, Z. et al. Chemical upcycling of polyethylene, polypropylene, and mixtures to high-value surfactants. *Science* **381**, 666-671 (2023).
22. Li, H. et al. Hydroformylation of pyrolysis oils to aldehydes and alcohols from polyolefin waste. *Science* **381**, 660-666 (2023).
23. Xu, Z. et al. Cascade degradation and upcycling of polystyrene waste to high-value chemicals. Proc. Natl. Acad. Sci. U.S.A. 119, e2203346119 (2022)..
24. Zeng, G., Su, Y., Jiang, J. & Huang, Z. Nitrogenative degradation of polystyrene waste. J. Am. Chem. Soc. 147, 2737-2746 (2025).
25. Martín, A.J., Mondelli, C., Jaydev, S.D. & Pérez-Ramírez, J. Catalytic processing of plastic waste on the rise. *Chem* **7**, 1487-1533 (2021).
26. Liu, Y., Ma, B., Tian, J. & Zhao, C. Coupled conversion of polyethylene and carbon dioxide catalyzed by a zeolite-metal oxide system. *Sci Adv* **10**, eadn0252 (2024).
27. ChemAnalyst. Toluene Market Size, Growth, Analysis & Forecast, 2035. https://www.chemanalyst.com/industry-report/toluene-market-665 (2023).
28. Zhang, F. et al. Polyethylene upcycling to long-chain alkylaromatics by tandem hydrogenolysis/aromatization. *Science* **370**, 437-441 (2020).
29. Liu, S., Kots, P.A., Vance, B.C., Danielson, A. & Vlachos, D.G. Plastic waste to fuels by hydrocracking at mild conditions. *Sci Adv* **7** (2021).
30. Chu, M. et al. Layered Double Hydroxide Derivatives for Polyolefin Upcycling. *J. Am. Chem. Soc.* **146**, 10655-10665 (2024).
31. Wang, Y.-Y. et al. Catalytic Hydrogenolysis of Polyethylene Under Reactive Separation. *ACS Catal.* **14**, 2084-2094 (2024).
32. Vance, B.C., Najmi, S. & Vlachos, D.G. Polystyrene Hydrogenolysis to High-Quality Lubricants Using Ni/SiO2. *ACS Catal.* **14**, 5389-5402 (2024).
33. Tang, M. et al. Upcycling of Polyamide Wastes to Tertiary Amines Using Mo Single Atoms and Rh Nanoparticles. *Angew Chem Int Ed Engl*, e202416436 (2024).
34. Gao, L. et al. Selective Upcycling of Polyethylene over Ru/H-ZSM-5 Bifunctional Catalyst into High-Quality Liquid Fuel at Mild Conditions. *ChemSusChem*, e202400598 (2024).
35. Ou, W. et al. Hydrogenation of the benzene rings in PET degraded chemicals over meso-HZSM-5 supported Ru catalyst. *J. Hazard. Mater.* **476**, 134964 (2024).
36. Fu, L. et al. Catalytic Pyrolysis of Waste Polyethylene Using Combined CaO

and Ga/ZSM-5 Catalysts for High Value-Added Aromatics Production. *ACS Sustainable Chem. Eng.* **10**, 9612-9623 (2022).
37. Wei, J. et al. Hydrodeoxygenation of Oxygen-Containing Aromatic Plastic Wastes to Liquid Organic Hydrogen Carriers. *Angew Chem Int Ed Engl* **62**, e202310505 (2023).
38. Wang, J. et al. Heterogeneous Diels-Alder tandem catalysis for converting cellulose and polyethylene into BTX. *J. Hazard. Mater.* **414**, 125418 (2021).
39. Eschenbacher, A. et al. Highly selective conversion of mixed polyolefins to valuable base chemicals using phosphorus-modified and steam-treated mesoporous HZSM-5 zeolite with minimal carbon footprint. *Appl. Catal., B* **309** (2022).
40. Liu, J. et al. Ni/HZSM-5 catalysts for hydrodeoxygenation of polycarbonate plastic wastes into cycloalkanes for sustainable aviation fuels. *Appl. Catal., B* **338** (2023).
41. Park, Y.-K. et al. Co-feeding effect of waste plastic films on the catalytic pyrolysis of Quercus variabilis over microporous HZSM-5 and HY catalysts. *Chem. Eng. J.* **378** (2019).
42. Ding, S., Hülsey, M.J., Pérez-Ramírez, J. & Yan, N. Transforming Energy with Single-Atom Catalysts. *Joule* **3**, 2897-2929 (2019).
43. Li, R. et al. Polystyrene Waste Thermochemical Hydrogenation to Ethylbenzene by a N-Bridged Co, Ni Dual-Atom Catalyst. *J. Am. Chem. Soc.* **145**, 16218-16227 (2023).
44. Chen, Y. et al. Single-Atom Catalysts: Synthetic Strategies and Electrochemical Applications. *Joule* **2**, 1242-1264 (2018).
45. Lee, K., Jing, Y., Wang, Y. & Yan, N. A unified view on catalytic conversion of biomass and waste plastics. *Nat Rev Chem* **6**, 635-652 (2022).
46. Xiong, H. et al. Engineering catalyst supports to stabilize PdOx two-dimensional rafts for water-tolerant methane oxidation. *Nat. Catal.* **4**, 830-839 (2021).
47. Zhang, Z. et al. Charge-Separated Pd(delta-)-Cu(delta+) Atom Pairs Promote CO(2) Reduction to C(2). *Nano Lett.* **23**, 2312-2320 (2023).
48. Hannagan, R.T., Giannakakis, G., Flytzani-Stephanopoulos, M. & Sykes, E.C.H. Single-Atom Alloy Catalysis. *Chem. Rev.* **120**, 12044-12088 (2020).
49. Wang, L. et al. The reformation of catalyst: From a trial-and-error synthesis to rational design. *Nano Research* **17**, 3261-3301 (2023).
50. Wang, Y. et al. Precise synthesis of dual atom sites for electrocatalysis. *Nano Research* **17**, 9397-9427 (2024).
51. Gan, T. & Wang, D. Atomically dispersed materials: Ideal catalysts in atomic era. *Nano Research* (2023).
52. Wu, X. et al. Tuning the d-Band Center of Co3O4 via Octahedral and Tetrahedral Codoping for Oxygen Evolution Reaction. *ACS Catal.* **14**, 5888-5897 (2024).
53. Zhang, M. et al. Surface Engineering on Ag-Decorated Co3O4 Electrocatalysts for Boosting Nitrate Reduction to Ammonia. *ACS Catal.* **14**,

11231-11242 (2024).
54. Duan, J. et al. Selective conversion of polyethylene wastes to methylated aromatics through cascade catalysis. *EES Catalysis* **1**, 529-538 (2023).
55. Genuino, H.C. et al. An improved catalytic pyrolysis concept for renewable aromatics from biomass involving a recycling strategy for co-produced polycyclic aromatic hydrocarbons. *Green Chem.* **21**, 3802-3806 (2019).
56. Zeng, L. et al. Recycling Valuable Alkylbenzenes from Polystyrene through Methanol-Assisted Depolymerization. *Angew Chem Int Ed Engl* **63**, e202404952 (2024).
57. Sullivan, K.P. et al. Mixed plastics waste valorization through tandem chemical oxidation and biological funneling. *Science* **378**, 207-211 (2022).